

AlloGen: Conformation-Selective Binder Generation with Differential State Scoring

Hanqun Cao,¹ Zachary Quinn,² Aastha Pal,² Sumi Kimura,² Jingjie Zhang,¹ Pheng Ann Heng,¹ Pranam Chatterjee^{2,3,†}

¹Department of Computer Science and Engineering, The Chinese University of Hong Kong

²Department of Bioengineering, University of Pennsylvania

³Department of Computer and Information Science, University of Pennsylvania

Correspondence: pranam@seas.upenn.edu

Model: <https://huggingface.co/ChatterjeeLab/AlloGen>



Abstract

Protein binder design has largely optimized for affinity alone, leaving conformational selectivity unaddressed: for allosteric targets such as kinases, nuclear receptors, and GPCRs, a binder that engages both active and inactive states provides no functional specificity regardless of how tightly it binds. We introduce **AlloGen**, a modular framework that decouples backbone generation from a learned state-selectivity scorer Q_θ , an SE(3)-invariant interface graph transformer trained via a two-phase curriculum that first learns interface geometry before imposing conformational discrimination. Because Q_θ is fully differentiable and generator-agnostic, it integrates with any backbone generator as a passive reranker or an active gradient-based guide without retraining. Across a diverse benchmark of proteins spanning multiple families and conformational mechanisms, AlloGen consistently identifies binders that preferentially recognize desired structural states while rejecting alternative conformations. Experimental validation on calmodulin further demonstrates that these computational selectivity signals translate to physical molecules, yielding *de novo* peptides that bind the desired holo conformation while exhibiting no detectable binding to the apo state. Together, these results establish conformational selectivity as a learnable property and provide a general framework for state-selective protein binder design.

1 Introduction

Proteins are molecular switches: their conformational transitions between distinct structural states govern signaling, catalysis, and regulation across virtually every protein family [1–4]. For therapeutically important targets such as kinases, nuclear receptors, and GPCRs, different conformational states correspond to distinct biological functions, and the design goal is therefore not merely binding affinity but conformational selectivity: stabilizing one functional state while actively disfavoring others [5–8]. This requirement is central to allosteric drug design, conformational biosensors, and synthetic biology switches [5, 9].

Recent generative models have transformed protein binder design, yet they share a common blind spot. At the sequence level, masked language modeling achieves state-of-the-art peptide binder design conditioned on target sequence [10], contrastive language models enable *de novo* peptide design to conformationally diverse targets [11], and multi-objective discrete diffusion has been applied to therapeutic peptide generation [12–15]. At the structural level, RFdiffusion establishes *de novo* design of functional protein binders at scale [16], PXDesign delivers fast and modular binder design with strong experimental success rates [17], Proteina-ComplexA scales atomistic binder design through generative pretraining and test-time compute [18], BoltzGen pursues universal binder design across protein families [19], and BindCraft co-folds target and binder by backpropagating through AlphaFold2 to produce experimentally validated binders without high-throughput screening [20, 21]. Despite this diversity, all existing methods share a fundamental limitation: they condition on a single receptor conformation and optimize for fit to that structure alone. A binder designed for one conformational state may bind equally well to an alternative state, defeating the purpose of state-selective targeting. Conventional scoring functions measure binding affinity but not differential affinity across states, and thus provide no signal for conformational selectivity.

To close this gap, we introduce **AlloGen**, a framework for conformationally selective protein binder design that decouples binder generation from selectivity evaluation (Figure 1). The central insight underlying AlloGen is that conformational selectivity is a learnable and transferable property of receptor–binder interfaces: once distilled into a differentiable scorer, it can be applied post hoc as either a reranker or an active guidance signal for diverse generative models. The core component of AlloGen is Q_θ , a lightweight SE(3)-invariant interface graph transformer trained on paired apo and holo receptor states to quantify state-specific binding preference. Because Q_θ is fully differentiable and generator-agnostic, it integrates seamlessly with existing protein design pipelines, enabling selectivity-guided generation through strategies ranging from best-of- K reranking to gradient-based refinement and sequential Monte Carlo sampling.

Using a benchmark of 65 targets spanning 15 protein families and 2,896 receptor–binder complexes, we show that Q_θ generalizes to held-out proteins where contact-based energy proxies fail uniformly and consistently improves conformational selectivity across diverse generator architectures. We further demonstrate that these computational selectivity signals translate to physical molecules through prospective experimental validation on calmodulin (CaM), where high-scoring designs yielded multiple holo-selective binders while a designated low-scoring negative control failed to bind. Together, these results establish conformational selectivity as a learnable design objective and provide a general framework for generating binders that recognize specific functional states rather than static protein structures.

2 Results

2.1 Q_θ recovers interface quality and conformational selectivity on held-out targets

To score conformational selectivity in a way that transfers across proteins, we developed Q_θ and evaluated it on eight out-of-distribution (OOD) test targets withheld during training (dataset construction and metrics are described in Section 4.9). Q_θ correlated with DockQ at $\bar{\rho}=0.520 \pm 0.010$

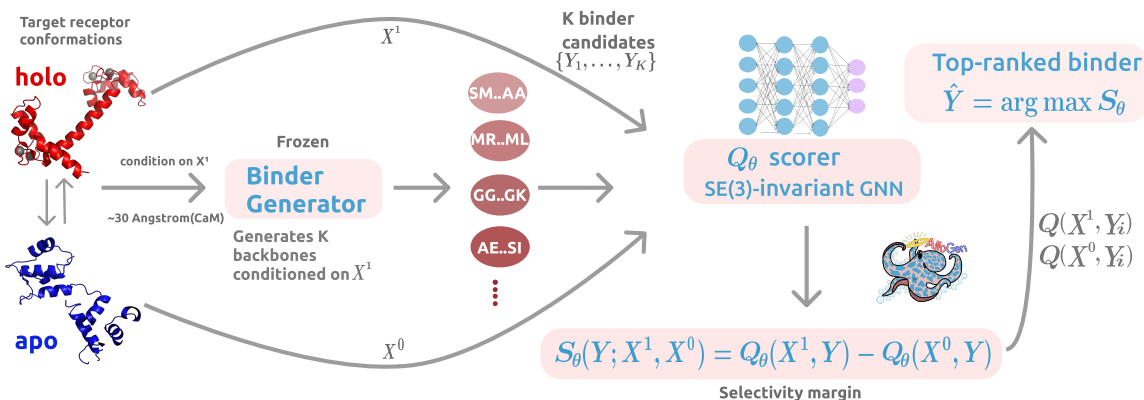


Figure 1: **AlloGen pipeline.** A frozen generator produces K binder backbones conditioned on the goal state X^1 (holo, blue); the trained scorer Q_θ evaluates each candidate against both X^1 and the undesired state X^0 (apo, red), and returns the top candidate \hat{Y} by selectivity margin $\Delta Q = Q_\theta(X^1, Y) - Q_\theta(X^0, Y)$. Q_θ is trained independently and plugs into any backbone generator without retraining.

over three training seeds, remaining positive on all eight targets and exceeding $\rho=0.5$ on four of them (Figure 2). We arrived at this configuration through three design choices, each of which we ablated. We first trained Q_θ with interface-quality regression alone (Phase 1), and while this produced a usable scorer, we reasoned that selectivity would benefit from an objective contrasting conformational states directly. Indeed, adding a Phase 2 of paired InfoNCE fine-tuning improved selectivity across all augmentation configurations (Figure 2a), with the gains concentrated on the hardest targets, where Phase 2 traded a slight drop on the two easiest proteins (BCL-2, ER α) for substantial improvement on the two hardest (Integrin, A $_{2A}$) and raised the eight-target mean from 0.481 to 0.520 (Supplementary Section S4, Table S4). An InfoNCE batch size of 256 was optimal, balancing cross-target negative diversity against optimization stability (Supplementary Section S4.2, Table S5). We next varied the training data and the input features. Augmenting the training set with GenDecoys, synthetic binders whose geometries span a broader region of interface space than rigid-body and FastRelax decoys, contributed the largest single improvement ($\Delta\bar{\rho}=+0.037$) by supplying harder negatives. Among the input features, ESM-2 embeddings [22] and binder-side dropout were each beneficial; removing ESM-2 lowered $\bar{\rho}$ on most targets and disabling binder dropout lowered it further, with the largest drops again on the hardest OOD proteins (Integrin, PAI-1, A $_{2A}$), so the combined configuration with both features performed best on all eight (Figure 2b).

2.2 Q_θ captures a state-specific signal that energy-based proxies miss

Strong rank correlation with DockQ does not by itself establish that Q_θ has learned conformation rather than generic binding quality. To test this, we first compared Q_θ against three contact-based proxies on the eight OOD targets (Table 1), reasoning that a conformational scorer must distinguish two receptor backbones presented with the same binder, which a single-interface score cannot. PRODIGY [23], total interface residue count, and cross-chain edge density all failed to track DockQ on average ($\bar{\rho}=+0.143, -0.154, -0.070$), whereas Q_θ reached $\bar{\rho}=0.520$ with all eight targets

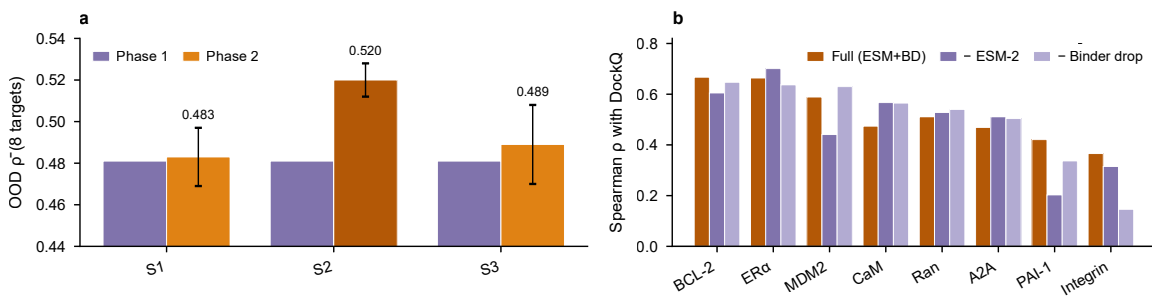


Figure 2: Q_θ selectivity performance. **(a)** Q_θ scoring performance ablation by data augmentation strategies and two phases; **(b)** Q_θ scoring performance ablation per target by different features.

positive, indicating that conformational selectivity is recoverable only from a representation trained on paired apo and holo geometry.

Table 1: Energy-based baselines vs. Q_θ on 8 OOD targets. Spearman ρ .

Target	n	PRODIGY	lface Size	Edge Dens.	Random	Q_θ
A _{2A} R	36	-0.230	-0.119	-0.092	-0.120	0.469 \pm .034
BCL-2	132	+0.160	-0.050	-0.082	-0.039	0.667 \pm .014
CaM	96	+0.199	-0.316	+0.014	+0.059	0.474 \pm .061
ER α	72	+0.551	-0.292	-0.036	+0.086	0.664 \pm .013
Integrin	60	-0.019	-0.195	+0.053	+0.076	0.366 \pm .085
MDM2	143	+0.163	-0.050	-0.130	-0.037	0.589 \pm .036
PAI-1	156	+0.058	+0.062	-0.146	-0.043	0.421 \pm .045
Ran	2268	+0.264	-0.270	-0.138	-0.018	0.511 \pm .065
Mean		+0.143	-0.154	-0.070	-0.005	0.520 \pm .010

To confirm that this preference was target-specific, we scored each target’s 50 vanilla binders against all eight OOD receptors. The diagonal of the resulting matrix exceeded its off-diagonal entries by a factor of 19.8 (Figure 3a), showing that Q_θ responds to the specific conformation it is given and not to generic shape complementarity. The same specificity was evident at the population level, where seven of eight targets showed a positive holo-minus-apo gap across 50 vanilla designs, BCL-2 separated the two states on every design under single-seed scoring, and CaM and MDM2 reached 100% and 98% holo preference under the three-seed ensemble (Figure 3b, Supplementary Section S4.3, Table S6). Integrin was the lone difficult case, with a gap of +0.001 and 52% holo preference, consistent with its lowest Spearman ρ . Finally, scoring designs against 11 conformations interpolated along the apo-to-holo path of CaM, we found that Q_θ increased monotonically toward holo ($\bar{\rho}=+0.518$, monotone in all ten cases), indicating that it had learned a continuous structural landscape across the transition (Table S7).

2.3 Selectivity guidance steers diverse generators toward state-selective binders

Having characterized Q_θ as a scorer, we asked whether it could also guide generation. We benchmarked it across three architecturally distinct generators (RFdiffusion [16], PXDesign [17], and

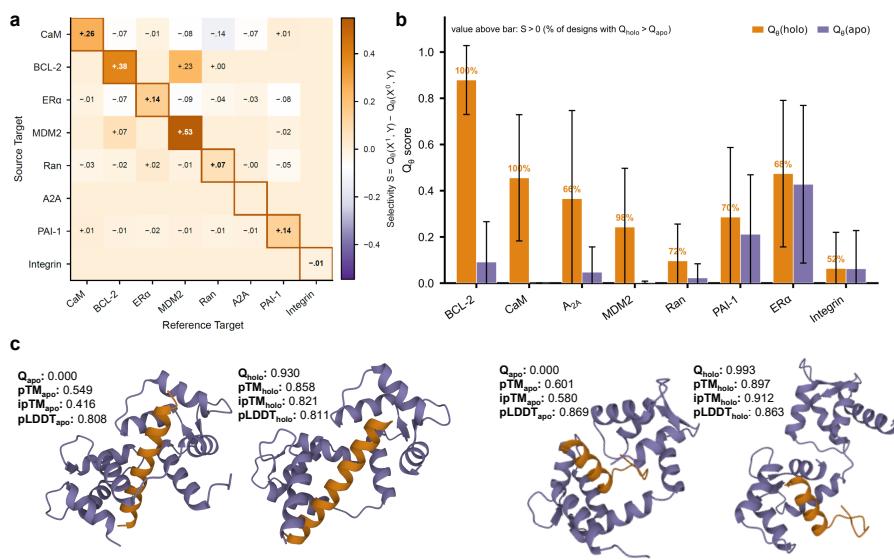


Figure 3: Q_θ conformational selectivity and CaM selectivity design. **(a)** Cross target selectivity matrix between Source Target (binders generated for) and the Reference Target (scored against). Zero values (0.00) have been omitted.; **(b)** Holo vs. apo Q_θ scores for 50 vanilla designs per target; **(c)** Selectivity-based design on CaM. Two case binders (orange) shown against the apo (1st and 3rd panels) and holo (2nd and 4th panels) receptor conformations (purple).

Proteina-ComplexA [18]) under vanilla sampling and four guidance strategies (classifier guidance, SMC, TDS, and Langevin refinement), giving 15 generator \times guidance combinations evaluated on the eight OOD targets, with each design scored by an ensemble of three independently trained Augmented-S2 checkpoints (Supplementary Section S5).

The benchmark revealed four consistent patterns (Table 2). Resampling-based guidance was strongest for every generator, with TDS and SMC ranked first or second throughout and classifier guidance rarely improving over vanilla sampling, indicating that trajectory-level reweighting transfers across architectures. Langevin refinement, by contrast, depended on the generator prior, improving the two structure-only generators (RFDiffusion from +0.249 to +0.314, Proteina-ComplexA from +0.213 to +0.267), which tolerate perturbing a completed backbone, and degrading PXDesign (+0.166 to +0.124), whose sequence-aware prior is destabilized when the co-designed interface geometry is perturbed. Target identity outweighed any method choice, with BCL-2 strongly selective across all 15 combinations ($\bar{S}=+0.781$) and Integrin, ER α , and PAI-1 weak under every combination. ER α was an informative exception, posting the second-highest scoring ρ (0.664) but the second-lowest design \bar{S} (+0.043), which places its bottleneck in generation rather than scoring, as current generators do not propose backbones that exploit its subtle H12 repositioning. The strength of vanilla sampling also conditioned what guidance could add. BCL-2, CaM, and MDM2 already carried substantial vanilla selectivity (means 0.71, 0.44, 0.32) that guidance amplified, whereas the five remaining targets sat near zero and acquired meaningful selectivity only under active guidance, making selectivity-guided generation essential for that group.

Table 2: End-to-end binder design selectivity (\bar{S}_{cons}) across 15 generator \times guidance combinations on 8 OOD targets. **Generators:** RF = RFdiffusion, PX = PXDesign, Pro = Proteina-ComplexA.

Guidance strategies: V = Vanilla, Cl = Classifier guidance, Lg = Langevin refinement, SM = SMC, TD = TDS. Bold indicates the best guidance per generator within each row.

Target	RF/V	RF/Cl	RF/Lg	RF/SM	RF/TD	PX/V	PX/Cl	PX/Lg	PX/SM	PX/TD	Pro/V	Pro/Cl	Pro/Lg	Pro/SM	Pro/TD	Mean
CaM	+0.455	+0.427	+0.677	+0.510	+0.367	+0.517	+0.521	+0.022	+0.545	+0.514	+0.338	+0.432	+0.429	+0.565	+0.374	+0.446
BCL-2	+0.787	+0.741	+0.806	+0.841	+0.880	+0.560	+0.561	+0.568	+0.868	+0.969	+0.774	+0.805	+0.826	+0.836	+0.898	+0.781
ER	+0.046	+0.054	+0.106	+0.325	+0.050	-0.031	-0.029	-0.027	+0.117	+0.029	-0.000	-0.000	-0.000	-0.000	+0.000	+0.043
A2A	+0.318	+0.332	+0.377	+0.760	+0.924	+0.023	+0.037	+0.048	+0.377	+0.445	-0.006	-0.004	-0.003	-0.000	-0.000	+0.242
MDM2	+0.238	+0.271	+0.366	+0.641	+0.769	+0.208	+0.227	+0.262	+0.590	+0.613	+0.506	+0.567	+0.598	+0.794	+0.883	+0.502
PAI-1	+0.073	+0.054	+0.061	+0.389	+0.262	-0.000	-0.000	-0.000	-0.000	-0.001	+0.053	+0.064	+0.069	+0.123	+0.757	+0.127
Ran	+0.074	+0.091	+0.108	+0.424	+0.485	+0.033	+0.056	+0.084	+0.446	+0.601	+0.081	+0.128	+0.204	+0.469	+0.662	+0.263
Integrin	+0.001	+0.006	+0.008	+0.013	+0.079	+0.015	+0.024	+0.033	+0.027	+0.185	-0.041	-0.002	-0.011	+0.017	+0.190	+0.038
Mean	+0.249	+0.247	+0.314	+0.488	+0.477	+0.166	+0.175	+0.124	+0.371	+0.419	+0.213	+0.249	+0.267	+0.350	+0.470	+0.305

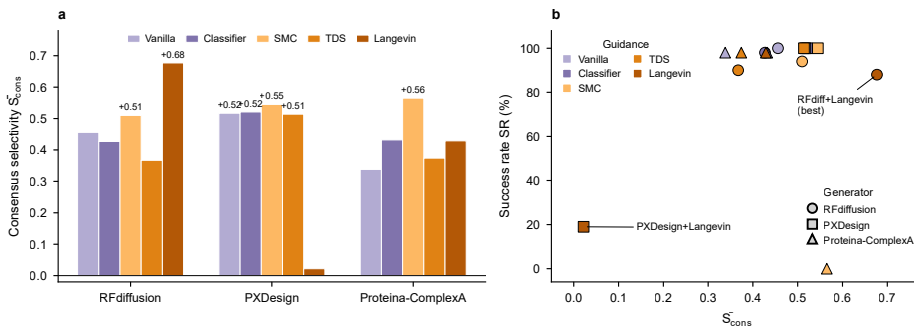


Figure 4: **Generation benchmark on CaM.** (a) Consensus selectivity \bar{S}_{cons} across 15 generation \times guidance approaches. (b) Selectivity vs. design success rate (designable \times selective) across all generator \times guidance combinations.

We then applied the full pipeline to CaM, a stringent test because its $\sim 30 \text{ \AA}$ apo-to-holo rearrangement on Ca^{2+} binding opens a hydrophobic peptide-binding cleft that is occluded in the apo state [24]. Fourteen of the 15 combinations gave positive mean selectivity, stable across the three training seeds (Table S8), and RFdiffusion with Langevin reached $\bar{S}_{\text{cons}} = +0.677$ at an 88% success rate combining designability and selectivity (Figure 4, Table S9). To explain why Langevin outperformed classifier guidance, we measured how Q_{θ} gradients behave under noise and found that their cosine similarity falls from 0.75 at low noise toward zero as the backbone is perturbed (Supplementary Section S5.2, Table S10); mapping this profile onto the RFdiffusion schedule placed classifier guidance in the uninformative-gradient regime for roughly 96% of its trajectory (Supplementary Section S5.3, Table S11), whereas Langevin operates only on fully denoised backbones and avoids it.

Q_{θ} was equally effective as a passive reranker. On the same vanilla pool, best-of-5 reached $\bar{S} = +0.787$ and best-of-10 reached +0.885, both exceeding Langevin (Supplementary Section S5.4, Table S12), and bootstrap resampling confirmed that the gain grew with pool size (Supplementary Section S5.5, Table S13). Reranking and Langevin are therefore complementary, the former scaling efficiently across a large pool and the latter providing per-design gains when candidates are expensive to sample, a trade-off quantified in our efficiency analysis (Supplementary Section S6), where per-method compute is reported in Supplementary Section S6 (Table S22) and per-complex

scorer latency in Supplementary Section S6.1. Two representative CaM designs illustrate the endpoint of the pipeline (Figure 3c), folding into compact helices that dock into the cleft exposed only after Ca^{2+} -induced lobe closure and scoring 0.930 and 0.993 against holo with near-zero apo scores, designs unreachable without explicit conformational supervision. Extended across all eight OOD targets, Langevin improved mean selectivity on seven while leaving native-contact recovery essentially unchanged ($\Delta\text{fNAT}_{\text{van}} \approx 0$ on the six targets with crystal-contact references; Supplementary Section S5.6, Table S14) and preserving backbone integrity, with zero Ramachandran outliers and a mean bond-length shift of 0.005 Å (Supplementary Section S5.7, Table S15) at a step size we set by sweeping η against $\text{C}\alpha$ displacement (Supplementary Section S5.8, Table S16).

Finally, we asked what the selectivity signal encodes by comparing AlloGen designs against scorers excluded from training. Three independent structural scorers agreed with Q_θ at the extremes. Boltz-2 ΔipTM correlated with Q_θ selectivity on A2A ($\rho=+0.500$) and CaM ($\rho=+0.349$) (Table S17), AlphaFold 3 confirmed holo preference on all 50 designs each for ALK and ER α (Table S18), and Rosetta InterfaceAnalyzer assigned the most favorable interface energy to BCL-2 (-9.1 REU) and the least to Integrin ($+39.1$ REU) (Supplementary Section S5.11, Table S19), each matching the Q_θ ranking at the strongest and weakest targets. Their disagreement on intermediate targets is itself informative, since Q_θ scores conformational selectivity while these tools score overall interface energy, quantities that need not coincide. A sequence-level check gave a complementary result. ProteinMPNN ΔNLL favored holo on all eight targets for vanilla designs ($p<0.05$; Supplementary Section S5.14, Table S20), confirming that holo bias is present in the backbones and detectable without Q_θ , yet Langevin reduced ΔNLL on five of eight targets while raising Q_θ , showing that the two metrics probe different axes and that Q_θ adds a geometric selectivity dimension orthogonal to sequence-recovery likelihood. The signal was also robust to degenerate generation, with only 10 of 482 CaM designs across nine pipelines scoring negative, all of them truncated or sterically infeasible backbones from a single pipeline and none an apo-selective design evading the scorer (Table S21). Together these analyses indicate that Q_θ encodes a physically grounded conformational selectivity signal that complements energy- and sequence-level scorers and is robust to degenerate generation.

2.4 AlloGen-designed peptides selectively bind holo calmodulin *in vitro*

To determine whether the predicted selectivity translated into measurable binding, we selected ten peptides from several generator-guidance combinations (RFdiffusion, Proteina-ComplexA, and their guided variants), ranked by predicted selectivity margin ($\Delta_q = q_{\text{holo}} - q_{\text{apo}}$), together with one low-scoring design as a negative control and the canonical Ca^{2+} -dependent M13 peptide as a positive control. We synthesized the panel and measured binding to holo CaM (prepared with CaCl_2) and apo CaM (prepared with EGTA) by bio-layer interferometry, immobilizing each peptide on a Twin-Strep biosensor and fitting association and dissociation against CaM at 0, 100, and 1000 nM to a 1:1 model (Figure 5).

Five of the ten peptides bound holo CaM (Table 3), with affinities from 46.6 nM to 1.06 μM and the two strongest in the nanomolar range. All five came from the high- Δ_q portion of the ranking (predicted margins 0.413 to 0.932), while the negative control selected for its lower margin ($\Delta_q = 0.228$) showed no detectable binding. The experiment matched the computational predictions, with high- Δ_q candidates yielding multiple holo-state binders and the low- Δ_q control failing to

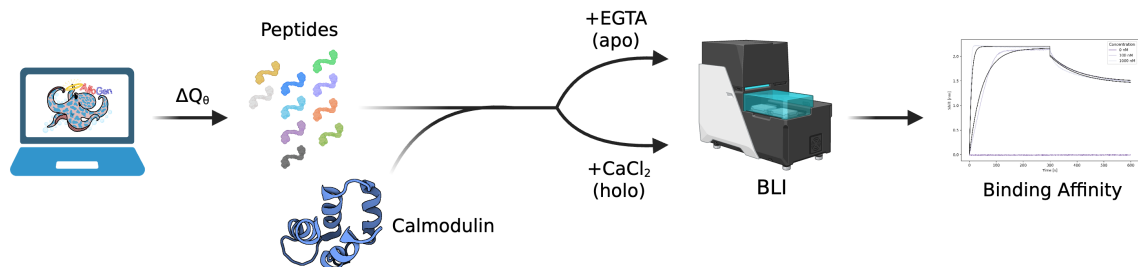


Figure 5: Experimental validation workflow for conformationally selective peptide binding to calmodulin (CaM). Candidate peptides were prioritized according to the predicted selectivity margin, $\Delta_q = q_{\text{holo}} - q_{\text{apo}}$, synthesized, and evaluated against apo and holo CaM in duplicate. Binding affinity was characterized by bio-layer interferometry (BLI), and equilibrium dissociation constants (K_D) were determined from kinetic fits.

Table 3: Sequences and experimental binding measurements for peptides evaluated against calmodulin (CaM). Binding affinities were measured by bio-layer interferometry against both holo and apo CaM. NB denotes no detectable binding. $\Delta_q = q_{\text{holo}} - q_{\text{apo}}$ is the difference between the predicted scores against holo and apo CaM.

Design	Sequence	Holo CaM K_D	Apo CaM K_D	Δ_q
rfdiff_vanilla__design_944	ATAAMIKTFQDVVVAAREAREK	46.6 nM	NB	0.413
rfdiff_vanilla__design_13	SEAFARAAVLAKARAAK	86.5 nM	NB	0.450
proteina_smc__smc_particle_0273	EGFKKLLKEALEIAK	413 nM	NB	0.932
rfdiff_vanilla__design_657	KVAEQAKQWILEMLAK	>1.00 μM	NB	0.930
rfdiff_langevin__design_25	EKLEALLREAGAARRAAKAAEAA	1.06 μM	NB	0.930
proteina_vanilla__design_0145	VDEGDGKIDLPESALLREKIK	NB	NB	0.993
rfdiff_langevin__design_330	SELTKEILKKAMEMT	NB	NB	0.905
proteina_vanilla__design_0376	AFGAEVKTPRTRFLDVLK	NB	NB	0.688
proteina_smc__smc_particle_0954	EEAARAAGLARLPRLLLLQAL	NB	NB	0.912
proteina_vanilla__design_0105 (Negative)	SEIAELRRNPEGDPETLREALAA	NB	NB	0.228
M13 positive control	KRRWKKNFIAVSAANRFKKISSSGAL	Bound	NB	-

bind, and every validated binder engaged holo CaM with no detectable binding to the apo state. These results provide direct evidence that the signal learned by Q_θ reflects a conformational preference that translates into measurable binding specificity.

3 Discussion

In this work, we introduce **AlloGen**, a framework for conformationally selective protein binder design that learns a transferable selectivity scorer, Q_θ , from paired structural states and applies it to existing binder generators as either a reranking or guidance signal. Across 65 targets spanning 15 protein families, Q_θ generalized to held-out proteins where contact-based energy proxies failed uniformly, and all 15 generator-guidance combinations achieved positive mean selectivity, reaching $\bar{S} = +0.885$ with best-of- K reranking.

Experimental validation demonstrated that these computational selectivity signals translate to

physical molecules. Five of ten synthesized peptides bound the desired holo conformation of calmodulin with affinities ranging from 46.6 nM to 1.06 μ M, while none exhibited detectable binding to the apo state. Moreover, all experimentally validated binders originated from the high- Δ_q region of the ranking, whereas a designated low- Δ_q negative-control peptide failed to bind. Together, these results establish that conformational selectivity can be learned from structural data and transferred to experimentally measurable binding specificity.

More broadly, AlloGen provides a general framework for designing molecules that recognize protein states rather than static protein structures. Future work will extend this approach to multi-state conformational landscapes, integrate selectivity directly into end-to-end sequence generation, and apply it to therapeutically relevant systems where biological activity depends on recognizing specific conformational states rather than simply maximizing binding affinity.

4 Methods

4.1 Problem Formulation

We consider a target protein that exists in two distinct conformational states: an *apo* (undesired) conformation X^0 and a *holo* (goal) conformation X^1 , both represented as backbone coordinate sets. Given a binder Y represented by its backbone coordinates, the *state-selectivity scoring problem* is to learn a function $Q_\theta : \mathcal{X} \times \mathcal{Y} \rightarrow (0, 1)$ such that for an X^1 -selective candidate Y :

$$Q_\theta(X^1, Y) \gg Q_\theta(X^0, Y), \quad (1)$$

while non-selective binders, apo-preferring binders, and non-binders are not required to satisfy this inequality. The training objective in Section 4.6 enforces this conditional behaviour through paired contrastive supervision rather than a global bias toward X^1 . Given a pretrained binder generator $p_\psi(Y | X^1)$, the *two-state binder design* task is to identify the most conformationally selective candidate $\hat{Y} = \arg \max_{Y^{(k)}} S_\theta(Y^{(k)}; X^1, \mathcal{N})$ over K samples $Y^{(k)} \sim p_\psi(\cdot | X^1)$, where S_θ is the selectivity margin defined in Section 4.7 and $\mathcal{N} = \{X^0\}$ is the set of undesired conformations.

4.2 Protein Backbone Representation and SE(3) Invariance

We represent each residue i by its C_α position $\mathbf{p}_i \in \mathbb{R}^3$ and a local backbone frame $R_i \in \text{SO}(3)$ constructed from the (N, C_α, C) triplet via Gram–Schmidt orthogonalization [21]. While \mathbf{p}_i and R_i themselves transform with global rigid motions, the pair (\mathbf{p}_i, R_i) defines a residue-local frame from which all inter-residue geometry can be expressed in an SE(3)-invariant way. For Q_θ to be physically meaningful, it must be SE(3)-invariant: $Q_\theta(gX, gY) = Q_\theta(X, Y)$ for all rigid motions $g \in \text{SE}(3)$, ensuring scores are independent of the global position and orientation of the complex. We enforce this by expressing all inter-residue geometry in the local frame of residue i : distances $\|\mathbf{p}_j - \mathbf{p}_i\|$, directions $R_i^\top(\mathbf{p}_j - \mathbf{p}_i)/\|\cdot\|$, and relative orientations $R_i^\top R_j$. Each of these quantities is invariant under rigid motions g applied jointly to both X and Y , so the resulting node and edge features, and hence Q_θ itself, are SE(3)-invariant.

4.3 DockQ as Interface Quality Proxy

DockQ [25] is a composite scalar $\in [0, 1]$ that measures protein–protein docking quality by combining the fraction of native contacts, interface RMSD, and ligand RMSD. We adopt DockQ as the supervision signal for Phase 1 training (Section 4.6), as it provides a geometrically grounded proxy for receptor–binder interface quality. Grounding Q_θ in DockQ before introducing any selectivity signal prevents degenerate solutions in Phase 2, where the model must distinguish between conformational states rather than simply predict binding quality. A DockQ value > 0.23 is the conventional threshold for an acceptable docking model [25].

4.4 Interface Graph Construction

To score receptor–binder complementarity in a way that is sensitive to local interface geometry rather than global protein shape, we represent each complex as a sparse graph over interface-proximal residues. Concretely, a receptor–binder complex (X, Y) is represented as an interface graph $\mathcal{G} = (\mathcal{V}, \mathcal{E})$, where \mathcal{V} contains residues from both X and Y with at least one inter-chain C_α contact within the cutoff as 8\AA , and edges connect all residue pairs within that cutoff.

Node features. Each node \mathbf{h}_i encodes four types of information. *Amino acid identity* is represented as a one-hot vector over 20 standard amino acids plus an unknown token, providing residue-level sequence identity. *Backbone torsion angles* φ , ψ , and ω are encoded via their sine and cosine values, yielding a smooth periodic representation of local backbone conformation. *Sidechain torsion angles* χ_1 and χ_2 are similarly encoded to capture rotameric states at the interface; residues without sidechain degrees of freedom are zero-padded. A *chain indicator* flag distinguishes receptor from binder residues. When available, per-residue ESM-2 embeddings [22] are projected and concatenated to these structural features, providing evolutionary context beyond local geometry.

Edge features. All edge features e_{ij} are computed in the local backbone frame of residue i , ensuring SE(3) invariance. *Geometric features* encode the inter-residue distance via a Gaussian RBF basis, the unit direction $R_i^\top (\mathbf{p}_j - \mathbf{p}_i) / \|\mathbf{p}_j - \mathbf{p}_i\|$, and the relative backbone orientation $R_i^\top R_j$, jointly capturing the full relative rigid-body relationship between residues. *Sequence separation* is encoded as a binned index difference within a chain and set to the maximum bin for inter-chain pairs, allowing the model to distinguish intra- from inter-chain interactions. A *same-chain indicator* flag further disambiguates receptor-receptor, binder-binder, and receptor-binder edges.

4.5 State-Selectivity Scorer Q_θ

Scoring conformational selectivity requires a model that assesses how well a binder backbone fits one receptor conformation relative to another in an SE(3)-invariant manner. To this end, Q_θ is implemented as a dense edge-biased graph transformer [26] that operates on SE(3)-invariant geometric features. Given node embeddings $\mathbf{H}^{(0)}$ and edge embeddings $\mathbf{E}^{(0)}$, the model applies

$L = 4$ transformer layers. At each layer ℓ , attention weights are computed as:

$$\alpha_{ij}^{(\ell)} = \frac{(\mathbf{h}_i^{(\ell)} W_Q)(\mathbf{h}_j^{(\ell)} W_K)^\top}{\sqrt{d_h}} + b_{ij}, \quad b_{ij} = \mathbf{e}_{ij} W_E \in \mathbb{R}, \quad (2)$$

$$\mathbf{h}_i^{(\ell+1)} = \mathbf{h}_i^{(\ell)} + \text{FFN} \left(\sum_j \text{softmax}_j(\alpha_{ij}^{(\ell)}) \cdot \mathbf{h}_j^{(\ell)} W_V \right), \quad (3)$$

where $W_E \in \mathbb{R}^{d_e \times 1}$ projects each edge embedding to a per-head scalar attention bias b_{ij} that is added directly to the dot-product logit (one such projection is learned per attention head). Edge embeddings are computed once and shared across all layers. After L layers, mean- and max-pooled node representations are concatenated to form $\mathbf{h}_{\text{pool}}^{(L)} = [\text{mean}_i \mathbf{h}_i^{(L)}; \text{max}_i \mathbf{h}_i^{(L)}]$ and passed through an MLP with sigmoid activation to produce:

$$Q_\theta(X, Y) = \sigma(\text{MLP}(\mathbf{h}_{\text{pool}}^{(L)})) \in (0, 1). \quad (4)$$

The bounded output yields a natural selectivity gap $Q_\theta(X^1, Y) - Q_\theta(X^0, Y) \in (-1, 1)$. Architectural hyperparameters and parameter count are reported in Supplementary Section S2.

4.6 Two-Phase Training of Q_θ

Directly optimizing Q_θ for conformational selectivity risks a degenerate solution where the model ignores receptor conformation entirely. We prevent this through a two-phase curriculum.

Phase 1: Interface Quality Regression. We first train Q_θ to predict interface quality as measured by DockQ [25]:

$$\mathcal{L}_q = \text{MSE}(Q_\theta(X, Y), d_{\text{DockQ}}(X, Y)). \quad (5)$$

Training data includes native holo complexes, apo mismatches, rigid-body decoys, and hard negatives described in Section 4.9. This phase establishes a geometrically grounded representation of receptor-binder fit, providing a stable initialization for Phase 2.

Phase 2: Selectivity Fine-Tuning. The central risk in fine-tuning for selectivity is that Q_θ collapses to target-specific biases, assigning high scores to any binder paired with a particular receptor regardless of conformation. We prevent this by fine-tuning on paired triplets (X^+, X^-, Y) where $X^+ = X^1$ and $X^- = X^0$ for the same binder Y , using a multi-negative InfoNCE loss [27] that includes both apo negatives (the same binder against its target’s apo conformation) and cross-target negatives (the anchor’s holo conformation paired with binders from other targets in the batch). The cross-target term forces the model to discriminate between the binder’s true holo partner and structurally unrelated holo receptors, preventing collapse to a fixed-receptor bias.

$$\begin{aligned} \mathcal{L}_{\text{NCE}} &= -\frac{1}{B} \sum_{i=1}^B \log \frac{\exp(Q_\theta(X_i^+, Y_i)/\tau)}{Z_i}, \quad (6) \\ Z_i &= \exp(Q_\theta(X_i^+, Y_i)/\tau) + \exp(Q_\theta(X_i^-, Y_i)/\tau) \\ &\quad + \sum_{\substack{k=1 \\ k \neq i}}^B \exp(Q_\theta(X_i^+, Y_k)/\tau). \end{aligned}$$

where τ is a temperature hyperparameter reported in Supplementary Section S2. The regression loss \mathcal{L}_q is dropped in Phase 2 to avoid conflicting gradient signals; this design choice is validated in Table 2.

Backbone-geometry augmentation. A third training design choice addresses the distribution shift between training and inference: at inference, Q_θ scores backbone-only binder designs without sequence identity or sidechain coordinates, whereas all training complexes have known sequences. To align the training distribution with this inference setting, we mask binder-side sequence features with probability p_{drop} :

$$\tilde{\mathbf{h}}_i^{\text{bnd}} = \begin{bmatrix} \mathbf{0}_{\text{AA}}, \sin \varphi_i, \cos \varphi_i, \sin \psi_i, \cos \psi_i, \\ \sin \omega_i, \cos \omega_i, \mathbf{0}_\chi, \mathbf{0}_{\text{ESM}}, 1 \end{bmatrix}. \quad (7)$$

where $\mathbf{0}_{\text{AA}}$, $\mathbf{0}_\chi$, and $\mathbf{0}_{\text{ESM}}$ replace the amino acid identity, sidechain torsion angles, and ESM-2 embeddings with zeros respectively. All backbone torsions and edge features are preserved, so Q_θ learns to rely on backbone geometry rather than sequence identity. The same masking decision is applied consistently to both X^+ and X^- within each training pair.

4.7 Selectivity-Guided Binder Design

Given K binder candidates $Y^{(1)}, \dots, Y^{(K)}$ sampled from the frozen generator $p_\psi(\cdot | X^1)$, each candidate is evaluated against both X^1 and X^0 by rigid placement onto their aligned structures. The *selectivity margin* is defined as:

$$S_\theta(Y; X^1, \mathcal{N}) = \text{logit}(Q_\theta(X^1, Y)) - \log \sum_{X^- \in \mathcal{N}} \exp(\text{logit}(Q_\theta(X^-, Y))). \quad (8)$$

where $\mathcal{N} = \{X^0\}$ is the set of undesired conformations. S_θ is high when Q_θ strongly prefers X^1 over X^0 , and negative when the binder scores similarly across states. The logit-space formulation extends naturally to multi-state targets with $|\mathcal{N}| > 1$. Candidates are filtered by minimum interface size and steric clash criteria before selection, and sequence design is performed with ProteinMPNN [28] on the selected backbone.

Gradient-based guidance. Because S_θ is differentiable with respect to backbone coordinates, it provides a gradient signal $\nabla_{\mathbf{x}} S_\theta$ that supports four guidance strategies. *Langevin backbone refinement* [29, 30] performs deterministic gradient ascent on S_θ for a completed backbone: $\mathbf{x}_{t+1} = \mathbf{x}_t + \eta \nabla_{\mathbf{x}} S_\theta(\mathbf{x}_t; X^1, \mathcal{N})$, where η is the step size; because Langevin operates on fully denoised backbones, gradients remain reliable throughout refinement. *Classifier guidance* [31] injects $\nabla_{\mathbf{x}} S_\theta$ into each denoising step to steer the diffusion trajectory toward high-selectivity regions, though gradient reliability degrades at high noise levels. *Twisted diffusion sampling* (TDS) [32] reweights diffusion particles by $\exp(S_\theta)$ at each timestep without modifying the denoising trajectory, preserving the generative prior more faithfully than classifier guidance. *Sequential Monte Carlo* (SMC) [32] iteratively resamples complete trajectories by S_θ across multiple generation rounds, progressively enriching the candidate pool and providing the most robust selectivity boost across diverse generator architectures. Detailed formulations and computational cost are provided in Supplementary Section S2.3 and S6.

4.8 Candidate Selection

To bridge from *in silico* selectivity to physical assays, we instantiate the full AlloGen pipeline as a candidate-triage funnel and carry the surviving designs to wet-lab synthesis. The funnel composes the generator–guidance machinery of Section 4.7 with a cascade of structure-prediction and geometric filters that are deliberately Q_θ -independent, so that the experimentally tested panel is not selected on the very signal it is meant to validate.

Dual-state hotspot conditioning. Both receptor states, the holo (goal) and apo (undesired) conformations, are processed to extract interface-proximal residues, and the *union* hotspot set is supplied to every generator. Conditioning on the state-invariant binding region, rather than a single conformation, ensures that backbones engage the functional interface while leaving the apo/holo discrimination to Q_θ .

Generation and selectivity scoring. We benchmark generator×guidance combinations at $N=50$ designs each, rank them by mean selectivity margin over their top-scoring designs, and promote the strongest baselines to large-scale generation at $N=1,024$ designs each.

Q_θ -independent structural filtering. Surviving backbones are sequence-designed with ProteinMPNN [28] (receptor chain fixed, four sequences per backbone at sampling temperature 0.1) and re-folded in *both* states with Boltz-2, producing per-state ipTM, pTM, and pLDDT. We retain designs whose buried surface area (computed with freesasa) exceeds 800 \AA^2 , whose holo-state ipTM exceeds 0.7, and whose selectivity margin satisfies $\Delta q \geq 0.3$, then collapse near-duplicates by clustering the retained sequences at 70% identity with CD-HIT.

Panel composition. From the clustered pool we assemble the 10-member panel submitted for synthesis: **8 experimental candidates** (the highest-margin guided designs, one per cluster) and **1 negative control** (a randomly drawn unguided design with near-zero margin $S \approx 0$), together with **1 positive control** (the M13 calmodulin-binding peptide). The negative control furnishes a built-in specificity test, a faithful selectivity signal should manifest as a measurable holo/apo affinity gap for the experimental candidates but *not* for the negative control, while the positive control confirms proper formation of the active (holo) receptor conformation. Complete provenance, generator settings, and selection logic are deferred to Supplementary Section S2.

4.9 Dataset Construction and Evaluation

Target selection. We curate 65 two-state proteins spanning 15 protein families and diverse conformational mechanisms (Table S2). Selection criteria are: (1) experimentally determined structures for both apo and holo conformational states, (2) at least three co-crystal structures with peptide or protein binders in the goal state, and (3) a structurally defined conformational change between states. Targets range from large-scale domain rearrangements (**CaM**: $\sim 30 \text{ \AA}$ apo-to-holo; **ABL1**: DFG-loop flip, $\sim 6.5 \text{ \AA}$ global) to subtle helix repositioning (**ER α** : H12 $\sim 10 \text{ \AA}$; **CDK2**: Cyclin A-induced). The dataset spans kinases (9), small GTPases (6), nuclear receptors (5), GPCRs and ion channels (6), proteases (6), and ten additional families, totalling 2,896 complexes across 65 targets.

Sample construction. Each complex yields 12 base training samples: 1 positive native holo complex (X^1, Y^{native}) with label 1.0; 1 negative apo-mismatch complex ($X_{\text{aligned}}^0, Y^{\text{native}}$) with label 0.0, where the apo receptor is Kabsch-aligned to the holo frame; and 10 rigid-body decoys at target C_α RMSD levels spanning 1–8 Å, with labels $\max(0, 1 - d_{\text{RMSD}}/4)$. Prior to augmentation, **FastRelax Neg.** are generated by constrained relaxation of binders placed on apo receptors, producing 959 hard negatives included in all configurations. Three augmentation types further enrich training: **Cross-family negatives** (Cross-fam) place native binders on structurally unrelated receptors; **conformational decoys** (Conf. decoys) apply Rosetta FastRelax repacking on the holo receptor to produce near-native hard negatives; and **generator decoys** (GenDecoys) are synthetic binders from structure-based generative models that provide diverse non-native interface geometries.

Dataset splits and configurations. All main results use the **target split**, in which targets are partitioned 51/6/8 across train, OOD validation, and OOD test, with CaM held out as the primary OOD design target (Table S2). The **Baseline** dataset comprises 51 training, 6 OOD validation (14-3-3, 14-3-3 σ , β_2 AR, Caspase-3, μ -opioid, Rac1), and 8 OOD test targets (CaM, BCL-2, ER α , MDM2, Ran, A_{2A}, PAI-1, Integrin); the **Augmented** dataset extends it with GenDecoys and cross-family negatives generated exclusively on training-set targets, precluding leakage into design evaluation. To isolate augmentation sources, we define three scoring configurations (Table S3): **S1** uses Baseline only, **S2** uses full Augmented data, and **S3** adds Cross-fam and Conf. decoys, withholding GenDecoys.

Metrics. We report Spearman ρ as rank correlation with DockQ, the selectivity gap $\bar{Q}^+ - \bar{Q}^-$ as mean holo vs. apo score, and best-of- K success rates. For design evaluation, we use ProteinMPNN ΔNLL and AlphaFold 3 ΔipTM as Q_θ -independent metrics, and report consensus selectivity \bar{S}_{cons} as the mean over three independently trained Q_θ checkpoints. Architecture and training hyperparameters are detailed in Supplementary Section S2.

4.10 Experimental Validation Protocol

Peptide selection. Candidate peptides were selected from multiple AlloGen generator–guidance combinations according to the predicted selectivity margin, $\Delta_q = q_{\text{holo}} - q_{\text{apo}}$. The experimental panel consisted of high- Δ_q candidates together with a designated low-scoring negative-control peptide. The skeletal myosin light-chain kinase M13 peptide (CPC Scientific, SIGN-010), a well-characterized Ca²⁺-dependent calmodulin-binding peptide, was included as a positive control.

Calmodulin preparation. Recombinant human calmodulin (MilliporeSigma, Cat. No. 208670) was used as the target protein. Holo CaM was prepared by supplementation with CaCl₂, whereas apo CaM was prepared by supplementation with EGTA to chelate free calcium. All other assay conditions were maintained identically between holo and apo measurements.

Bio-layer interferometry. Binding measurements were performed by Adaptyv Bio using bio-layer interferometry (BLI) on a Gator Bio Pro instrument. Designed peptides were immobilized on Twin-Strep-compatible biosensors through a Twin-Strep tag according to the manufacturer’s workflow. Following ligand loading and baseline equilibration, biosensors were transferred into wells containing serial dilutions of CaM (0, 100, and 1000 nM) to record association kinetics,

followed by transfer into assay buffer to monitor dissociation. All measurements were performed in duplicate.

Data analysis. Sensorgrams were reference-subtracted using control sensors and buffer-only wells. Association rate constants (k_{on}), dissociation rate constants (k_{off}), and equilibrium dissociation constants (K_D) were obtained by fitting the processed sensorgrams to a 1:1 binding model. Designs exhibiting concentration-dependent binding responses were classified as binders and assigned fitted K_D values, whereas designs that failed to produce measurable binding responses were reported as no binding detected (NB). Conformational selectivity was assessed by comparing binding to holo and apo CaM under identical assay conditions.

Data and Code Availability

All data code required to evaluate AlloGen is publicly available at <https://huggingface.co/ChatterjeeLab/AlloGen>. The repository includes an interactive Google Colab notebook for running AlloGen on user-defined targets.

Acknowledgments

We thank the experimental team of the Chatterjee Laboratory for assistance with peptide design validation and helpful discussions throughout this project. We especially thank Adaptic Bio for performing bio-layer interferometry measurements and assisting with experimental characterization of candidate binders. Finally, we thank Lauren Hong for providing the model logo.

This research was supported by a grant from the High-throughput Institute for Discovery (HIT-ID) at the University of Pennsylvania to the laboratory of Pranam Chatterjee. The work described in this paper was also partially supported by the Research Grants Council of the Hong Kong Special Administrative Region, China, under Project T45-401/22-N.

Author Contributions Statement

H.C. and P.C. conceived the project. H.C. led model development, dataset construction, computational experiments, and manuscript preparation. Z.Q. and S.K. led experimental validation efforts with Adaptic Bio. A.P., Y.K., and J.Z. assisted with experimental validation, computational analyses, and result interpretation. P.A.H. and P.C. supervised the study. H.C. and P.C. wrote the manuscript with input from all authors.

Competing Interests Statement

P.C. is a co-founder of Gameto, Inc., UbiquiTx, Inc., AtomBioworks, Inc., and Recognition Bio, Inc., and advises companies involved in biologics and therapeutic development. P.C.'s interests are reviewed and managed by the University of Pennsylvania in accordance with its conflict-of-interest policies. The remaining authors declare no competing interests.

References

- [1] Stefan W Vetter and Estelle Leclerc. Novel aspects of calmodulin target recognition and activation. *European Journal of Biochemistry*, 270(3):404–414, 2003.
- [2] Jeung-Hoi Ha and Stewart N Loh. Protein conformational switches: from nature to design. *Chemistry—A European Journal*, 18(26):7984–7999, 2012.
- [3] Thomas R Weikl and Fabian Paul. Conformational selection in protein binding and function. *Protein Science*, 23(11):1508–1518, 2014.
- [4] Ruth Nussinov. Introduction to protein ensembles and allostery, 2016.
- [5] Gozde Kar, Ozlem Keskin, Attila Gursoy, and Ruth Nussinov. Allostery and population shift in drug discovery. *Current opinion in pharmacology*, 10(6):715–722, 2010.
- [6] RSK Vijayan, Peng He, Vivek Modi, Krisna C Duong-Ly, Haiching Ma, Jeffrey R Peterson, Roland L Dunbrack Jr, and Ronald M Levy. Conformational analysis of the dfg-out kinase motif and biochemical profiling of structurally validated type ii inhibitors. *Journal of medicinal chemistry*, 58(1):466–479, 2015.
- [7] Douglas J Kojetin and Thomas P Burris. Small molecule modulation of nuclear receptor conformational dynamics: implications for function and drug discovery. *Molecular pharmacology*, 83(1):1–8, 2013.
- [8] Paolo Conflitti, Edward Lyman, Mark SP Sansom, Peter W Hildebrand, Hugo Gutiérrez-de Terán, Paolo Carloni, T Bertie Ansell, Shuguang Yuan, Patrick Barth, Anne S Robinson, et al. Functional dynamics of g protein-coupled receptors reveal new routes for drug discovery. *Nature Reviews Drug Discovery*, 24(4):251–275, 2025.
- [9] Robert A Langan, Scott E Boyken, Andrew H Ng, Jennifer A Samson, Galen Dods, Alexandra M Westbrook, Taylor H Nguyen, Marc J Lajoie, Zibo Chen, Stephanie Berger, et al. De novo design of bioactive protein switches. *Nature*, 572(7768):205–210, 2019.
- [10] Leo Tianlai Chen, Zachary Quinn, Madeleine Dumas, Christina Peng, Lauren Hong, Moises Lopez-Gonzalez, Alexander Mestre, Rio Watson, Sophia Vincoff, Lin Zhao, et al. Target sequence-conditioned design of peptide binders using masked language modeling. *Nature Biotechnology*, pages 1–9, 2025.
- [11] Suhaas Bhat, Kalyan Palepu, Lauren Hong, Joey Mao, Tianzheng Ye, Rema Iyer, Lin Zhao, Tianlai Chen, Sophia Vincoff, Rio Watson, et al. De novo design of peptide binders to conformationally diverse targets with contrastive language modeling. *Science Advances*, 11(4): eadr8638, 2025.
- [12] Sophia Tang, Yinuo Zhang, and Pranam Chatterjee. Peptune: De novo generation of therapeutic peptides with multi-objective-guided discrete diffusion. In *Forty-second International Conference on Machine Learning*, 2025. URL <https://openreview.net/forum?id=FQoy1Y1Hd8>.
- [13] Sophia Vincoff, Oscar Davis, Ismail Ilkan Ceylan, Alexander Tong, Joey Bose, and Pranam

- Chatterjee. Soapia: Siamese-guided generation of off target-avoiding protein interactions with high target affinity. In *ICML 2025 Generative AI and Biology (GenBio) Workshop*, 2025.
- [14] Hanqun Cao, Haosen Shi, Chenyu Wang, Sinno Jialin Pan, and Pheng-Ann Heng. GLID²: A gradient-free lightweight fine-tune approach for discrete biological sequence design. In *The Thirty-ninth Annual Conference on Neural Information Processing Systems*, 2025. URL <https://openreview.net/forum?id=AHjspi4R22>.
- [15] Hanqun Cao, Aastha Pal, Sophia Tang, Yinuo Zhang, Jingjie Zhang, Pheng-Ann Heng, and Pranam Chatterjee. TD3b: Transition-directed discrete diffusion for allosteric binder generation. In *Forty-Third International Conference on Machine Learning*, 2026. URL <https://openreview.net/forum?id=r2nuhKd6vr>.
- [16] Joseph L Watson, David Juergens, Nathaniel R Bennett, Brian L Trippe, Jason Yim, Helen E Eisenach, Woody Ahern, Andrew J Borst, Robert J Ragotte, Lukas F Milles, et al. De novo design of protein structure and function with rfdiffusion. *Nature*, 620(7976):1089–1100, 2023.
- [17] Protenix Team, Milong Ren, Jinyuan Sun, Jiaqi Guan, Cong Liu, Chengyue Gong, Yuzhe Wang, Lan Wang, Qixu Cai, Xinshi Chen, et al. Pxdesign: Fast, modular, and accurate de novo design of protein binders. *bioRxiv*, 2025.
- [18] Kieran Didi, Zuobai Zhang, Guoqing Zhou, Danny Reidenbach, Zhonglin Cao, Sooyoung Cha, Tomas Geffner, Christian Dallago, Jian Tang, Michael M. Bronstein, Martin Steinegger, Emine Kucukbenli, Arash Vahdat, and Karsten Kreis. Scaling atomistic protein binder design with generative pretraining and test-time compute. In *The Fourteenth International Conference on Learning Representations*, 2026. URL <https://openreview.net/forum?id=qmCpJtFZra>.
- [19] Hannes Stark, Felix Faltings, MinGyu Choi, Yuxin Xie, Eunsu Hur, Timothy O’Donnell, Anton Bushuiev, Talip Uçar, Saro Passaro, Weian Mao, et al. Boltzgen: Toward universal binder design. *bioRxiv*, 2025.
- [20] Martin Pacesa, Lennart Nickel, Christian Schellhaas, Joseph Schmidt, Ekaterina Pyatova, Lucas Kissling, Patrick Barendse, Jagrity Choudhury, Srajan Kapoor, Ana Alcaraz-Serna, et al. One-shot design of functional protein binders with bindcraft. *Nature*, 646(8084):483–492, 2025.
- [21] John Jumper, Richard Evans, Alexander Pritzel, Tim Green, Michael Figurnov, Olaf Ronneberger, Kathryn Tunyasuvunakool, Russ Bates, Augustin Žídek, Anna Potapenko, et al. Highly accurate protein structure prediction with alphafold. *nature*, 596(7873):583–589, 2021.
- [22] Zeming Lin, Halil Akin, Roshan Rao, Brian Hie, Zhongkai Zhu, Wenting Lu, Nikita Smetanin, Robert Verkuil, Ori Kabeli, Yaniv Shmueli, et al. Evolutionary-scale prediction of atomic-level protein structure with a language model. *Science*, 379(6637):1123–1130, 2023.
- [23] Li C Xue, João Pglm Rodrigues, Panagiotis L Kastiris, Alexandre Mjj Bonvin, and Anna Van-gone. Prodigy: a web server for predicting the binding affinity of protein–protein complexes. *Bioinformatics*, 32(23):3676–3678, 2016.

- [24] Anna Crivici and Mitsuhiko Ikura. Molecular and structural basis of target recognition by calmodulin. *Annual review of biophysics and biomolecular structure*, 24:85–116, 1995.
- [25] Sankar Basu and Björn Wallner. Dockq: a quality measure for protein-protein docking models. *PloS one*, 11(8):e0161879, 2016.
- [26] Ashish Vaswani, Noam Shazeer, Niki Parmar, Jakob Uszkoreit, Llion Jones, Aidan N Gomez, Łukasz Kaiser, and Illia Polosukhin. Attention is all you need. *Advances in neural information processing systems*, 30, 2017.
- [27] Aaron van den Oord, Yazhe Li, and Oriol Vinyals. Representation learning with contrastive predictive coding. *arXiv preprint arXiv:1807.03748*, 2018.
- [28] Justas Dauparas, Ivan Anishchenko, Nathaniel Bennett, Hua Bai, Robert J Ragotte, Lukas F Milles, Basile IM Wicky, Alexis Courbet, Rob J de Haas, Neville Bethel, et al. Robust deep learning-based protein sequence design using proteinmpnn. *Science*, 378(6615):49–56, 2022.
- [29] Yang Song, Jascha Sohl-Dickstein, Diederik P Kingma, Abhishek Kumar, Stefano Ermon, and Ben Poole. Score-based generative modeling through stochastic differential equations. In *International Conference on Learning Representations*, 2021. URL <https://openreview.net/forum?id=PXTIG12RRHS>.
- [30] Max Welling and Yee W Teh. Bayesian learning via stochastic gradient langevin dynamics. In *Proceedings of the 28th international conference on machine learning (ICML-11)*, pages 681–688, 2011.
- [31] Prafulla Dhariwal and Alexander Nichol. Diffusion models beat gans on image synthesis. *Advances in neural information processing systems*, 34:8780–8794, 2021.
- [32] Luhuan Wu, Brian Trippe, Christian Naesseth, David Blei, and John P Cunningham. Practical and asymptotically exact conditional sampling in diffusion models. *Advances in Neural Information Processing Systems*, 36:31372–31403, 2023.
- [33] Zhenqiao Song, Tianxiao Li, Lei Li, and Martin Renqiang Min. PPDiff: Diffusing in hybrid sequence-structure space for protein-protein complex design. In *Forty-second International Conference on Machine Learning*, 2025. URL <https://openreview.net/forum?id=gTYzm0Qchr>.
- [34] Tong Chen, Zachary Quinn, Yinuo Zhang, and Pranam Chatterjee. moppit-v3: Motif-specific peptides generated via multi-objective-guided discrete flow matching. In *NeurIPS 2025 AI for Science Workshop*.
- [35] Sophia Tang, Yuchen Zhu, Molei Tao, and Pranam Chatterjee. Tr2-d2: Tree search guided trajectory-aware fine-tuning for discrete diffusion. *arXiv preprint arXiv:2509.25171*, 2025.
- [36] Tong Chen, Yinuo Zhang, and Pranam Chatterjee. Areuredi: Annealed rectified updates for refining discrete flows with multi-objective guidance. *arXiv preprint arXiv:2510.00352*, 2025.
- [37] Sophia Tang, Yinuo Zhang, Alexander Tong, and Pranam Chatterjee. Gumbel-softmax score and flow matching for discrete biological sequence generation. 2025.

- [38] Joost Schymkowitz, Jesper Borg, Francois Stricher, Robby Nys, Frederic Rousseau, and Luis Serrano. The foldx web server: an online force field. *Nucleic acids research*, 33(suppl_2): W382–W388, 2005.
- [39] Chloe Hsu, Robert Verkuil, Jason Liu, Zeming Lin, Brian Hie, Tom Sercu, Adam Lerer, and Alexander Rives. Learning inverse folding from millions of predicted structures. In *International conference on machine learning*, pages 8946–8970. PMLR, 2022.
- [40] Xiao Wang, Sean T Flannery, and Daisuke Kihara. Protein docking model evaluation by graph neural networks. *Frontiers in Molecular Biosciences*, 8:647915, 2021.
- [41] Xiaotong Xu and Alexandre MJJ Bonvin. Deeprank-gnn-esm: a graph neural network for scoring protein–protein models using protein language model. *Bioinformatics advances*, 4(1):vbad191, 2024.
- [42] Bowen Jing, Bonnie Berger, and Tommi Jaakkola. Alphafold meets flow matching for generating protein ensembles. In *Forty-first International Conference on Machine Learning*, 2024. URL <https://openreview.net/forum?id=rs8Sh2UASst>.
- [43] Yogesh Kalakoti and Björn Wallner. Afsample2 predicts multiple conformations and ensembles with alphafold2. *Communications biology*, 8(1):373, 2025.
- [44] Josh Abramson, Jonas Adler, Jack Dunger, Richard Evans, Tim Green, Alexander Pritzel, Olaf Ronneberger, Lindsay Willmore, Andrew J Ballard, Joshua Bambrick, et al. Accurate structure prediction of biomolecular interactions with alphafold 3. *Nature*, 630(8016):493–500, 2024.
- [45] P Benjamin Stranges and Brian Kuhlman. A comparison of successful and failed protein interface designs highlights the challenges of designing buried hydrogen bonds. *Protein Science*, 22(1):74–82, 2013.
- [46] Sarel J Fleishman, Timothy A Whitehead, Damian C Ekiert, Cyrille Dreyfus, Jacob E Corn, Eva-Maria Strauch, Ian A Wilson, and David Baker. Computational design of proteins targeting the conserved stem region of influenza hemagglutinin. *Science*, 332(6031):816–821, 2011.
- [47] James J Havranek and Pehr B Harbury. Automated design of specificity in molecular recognition. *Nature structural biology*, 10(1):45–52, 2003.
- [48] Yang Xue, Hong Wang, Jun Li, Jianguo Hu, Zhiyuan Chen, Zhi Zheng, Lihang Liu, Kunrui Zhu, Jingzhou He, Huanzhang Gong, et al. State-specific peptide design targeting g protein-coupled receptors. *Journal of Chemical Information and Modeling*, 65(20):11425–11438, 2025.
- [49] Bowen Jing, Anna Sappington, Mihir Bafna, Ravi Shah, Adrina Tang, Rohith Krishna, Adam Klivans, Daniel J Diaz, and Bonnie Berger. Generating functional and multistate proteins with a multimodal diffusion transformer. *bioRxiv*, 2025.

Supplementary Information

S1 Related Work

S1.1 Structure-Based Binder Design

Deep generative models have transformed structure-based protein binder design. RFdiffusion [16] generates binder backbones conditioned on a fixed target surface via backbone diffusion, followed by sequence design with ProteinMPNN [28]. PPDiff [33] and PXDesign [17] extend this to joint sequence-structure generation, while Proteina-ComplexA [18] employs atomistic flow matching to produce full-atom binder complexes. On the sequence side, a growing body of work generates binder sequences through discrete diffusion and language model objectives [10–15, 34–37]. Despite their diversity, all of these methods share a fundamental constraint: they condition on a single, static receptor conformation and optimize for binding quality without any mechanism for conformational selectivity. AlloGen is designed to be complementary that its modular scorer Q_θ can rerank or guide candidates produced by any of these generators.

S1.2 Protein–Protein Interface Scoring

Physics-based methods such as FoldX [38] and PRODIGY [23] estimate binding free energies, and inverse folding models such as ProteinMPNN [28] and ESM-IF [39] serve as zero-shot affinity proxies. GNN-based scorers including GNN-DOVE [40] and DeepRank-GNN-esm [41] learn interface quality from structural features, but are designed for docking re-ranking rather than conformational discrimination. Critically, all of these methods measure affinity rather than differential affinity, and provide no signal for selecting one conformational state over another. Q_θ departs from this paradigm through its two-phase curriculum, which prevents the degenerate solution of ignoring receptor conformation. Moreover, its logit-space selectivity margin that explicitly reasons about score differences across states.

S1.3 Conformational Selectivity: Sampling, Design, and Negative Design

Achieving conformational selectivity requires both characterizing the conformational landscape and engineering molecules that exploit it. On the characterization side, AlphaFlow [42] uses flow matching to generate structural ensembles, AFsample2 [43] diversifies predictions via MSA sub-sampling, and AlphaFold 3 [44] extends structure prediction to biomolecular complexes. These methods map the conformational space but do not address the inverse problem of designing binders that discriminate between states. On the design side, negative design has a long history in computational protein engineering [45, 46], and multi-state design in Rosetta [47] optimizes sequences across multiple conformations. However, these approaches operate at the sequence level and do not provide a differentiable scoring signal compatible with modern backbone generators. Contrastive objectives inspired by InfoNCE [27] have been applied to molecular representation learning, and classifier guidance [31] and TDS [32] enable gradient-based steering of diffusion models, mechanisms we directly adopt. Concurrent work by Xue et al. [48] targets state-specific peptide design for GPCRs via a conformation-specific folding filter, and ProDiT [49] introduces multi-state structure diffusion. AlloGen unifies these threads: it learns a generalizable selectivity

scorer through contrastive training, applies it as a gradient-based guide across architecturally diverse generators, and demonstrates generalization across 15 protein families.

S2 Implementation Details

S2.1 Feature Computation

Backbone frames. Backbone frames $R_i \in SO(3)$ are constructed from the (N, C_α, C) triplet of each residue using the Gram–Schmidt procedure. Torsion angles (φ, ψ, ω) are computed from four consecutive backbone atoms using the standard dihedral angle formula. At chain termini, missing torsion angles are set to zero.

RBF distance encoding. The 16-dimensional RBF encoding of distance d uses Gaussian basis functions $\exp(-\gamma(d - \mu_k)^2)$ with centres μ_k evenly spaced from 2 to 12 Å and width $\gamma = 1.5$.

S2.2 Model and Training Hyperparameters

Model size. The InterfaceGNN scorer has $\sim 898\text{K}$ trainable parameters: 4 graph transformer layers with hidden dimension 128, 8 attention heads, query/key/value and edge bias projections, and a 3-layer scoring MLP.

Training hyperparameters. Hyperparameters for both training phases are listed in Table S1.

Table S1: Training hyperparameters for the two-phase curriculum.

Hyperparameter	Phase 1	Phase 2
Epochs	40	15
Learning rate	5×10^{-4}	4×10^{-5}
Weight decay	10^{-3}	10^{-3}
Batch size	512	256
Warmup steps	100	—
Loss	MSE (\mathcal{L}_q)	InfoNCE (\mathcal{L}_q dropped)
InfoNCE τ	—	0.1
LR schedule	Cosine	Cosine
Dropout	0.1	0.1
Binder dropout	0.3	0.3

Guidance hyperparameters. For RFdiffusion classifier guidance, Q_θ is used as a guiding potential with weight $\omega=1.0$ and global `guide_scale = 5.0`, constant decay schedule, and 200 denoising steps. For PXDesign classifier guidance, guidance scale 1.0 is applied during diffusion progress fractions $[0.1, 0.8]$, with noise-fraction-proportional decay within that window. Langevin refinement uses step size $\eta=0.05$ and 100 gradient steps for RFdiffusion backbones, or $\eta=0.01$ and 100 steps for PXDesign. TDS uses $N=16$ particles and $R=4$ resampling rounds, retaining the top 50% of particles each round.

S2.3 Guidance Formulations

All four guidance strategies exploit the differentiability of $S_\theta(Y; X^1, \{X^0\})$ with respect to binder backbone coordinates $\mathbf{x} = \{\mathbf{p}_i\}_{i \in Y}$.

Langevin backbone refinement ([29, 30]). Given a generated backbone \mathbf{x}_0 , we perform T steps of gradient ascent on the selectivity margin:

$$\mathbf{x}_{t+1} = \mathbf{x}_t + \eta \nabla_{\mathbf{x}} S_\theta(\mathbf{x}_t; X^1, \{X^0\}), \quad t = 0, \dots, T-1, \quad (\text{S1})$$

where η is the step size. This operates on fully denoised backbones, avoiding the noisy-gradient regime.

Classifier guidance ([31]). During diffusion denoising, we inject the Q_θ gradient into each denoising step:

$$\hat{\epsilon}_t = \epsilon_\psi(\mathbf{x}_t, t) - \omega \sigma_t \nabla_{\mathbf{x}_t} \log Q_\theta(X^1, \mathbf{x}_t), \quad (\text{S2})$$

where ϵ_ψ is the denoiser, ω the guidance weight, and σ_t the noise level at timestep t .

Twisted diffusion sampling (TDS) ([32]). TDS uses N particles $\{\mathbf{x}_t^{(n)}\}_{n=1}^N$ with importance weights $w_t^{(n)} \propto Q_\theta(X^1, \hat{\mathbf{x}}_0^{(n)})$ computed from the denoised prediction at each timestep. Multinomial resampling is applied when the effective sample size $\text{ESS} = (\sum_n w_n)^2 / \sum_n w_n^2$ drops below $N/2$.

Sequential Monte Carlo (SMC) ([32]). SMC extends TDS with multiple resampling rounds: after generating N complete trajectories, the top fraction by S_θ seeds the next round, iteratively enriching the candidate pool toward high-selectivity designs.

S3 Dataset Construction

The dataset comprises 2,896 complexes across 65 two-state protein targets in 15 families. Each complex yields 12 training samples: 1 native holo labeled 1.0, 1 apo mismatch labeled 0.0, and 10 rigid-body decoys with labels $\max(0, 1 - d_{\text{RMSD}}/4)$, plus 959 FastRelax-based hard negatives with mean label 0.304. Interface graphs contain 34.7 ± 19.7 nodes, ranging from 3 to 128 with a median of 29, comprising 18.1 ± 9.8 receptor and 16.6 ± 11.0 binder residues. The target split assigns 51 targets to training, 6 to OOD validation, and 8 to OOD test with CaM held out, yielding 30,623 samples split as 23,640 training, 4,020 validation, and 2,963 test (Table S2). Linked targets such as SRC and SRC-SH2 are forced into the same partition. All scoring experiments use the S2-augmented configuration totalling 39,867 training samples; ablations across S1/S2/S3 are detailed in Table S3.

S4 Extended Q_θ Results

All results in this section use the S2 configuration with the target split (Table S2), ESM-2 encoder, and binder-dropout rate $p=0.3$, consistent with the experimental setup in Section 2.1. The suffix S1/S2/S3 denotes the dataset augmentation configuration as defined in Table S3.

Table S2: **Target split.** 51/6/8 train/val/test partition across 15 protein families. CaM is moved to the OOD test set as the primary design target; ALK is moved to training.

Family	Train (51)	Val OOD (6)	Test OOD (8)
Kinase (9)	ABL1, ALK , Aurora A, BRAF, CDK2, EGFR, GRK2, SRC, SRC-SH2	—	—
Small GTPase (6)	Arf1, CDC42, KRAS, RhoA	Rac1	Ran
Nuclear Receptor (5)	AR, GR, PPAR γ , RXR α	—	ER α
GPCR/Ion Ch. (6)	CFTR, KcsA, nAChR	β_2 AR, μ -opioid	A $_2$ A
Phosphatase (4)	Calcineurin, PP2A, PTP1B, SHP2	—	—
Protease (6)	HIV-PR, MMP-2, M ^{pro} , Thrombin, USP7	Caspase-3	—
BCL-2 (2)	BCL-xL	—	BCL-2
14-3-3 (2)	—	14-3-3, 14-3-3 σ	—
Ca sensor (3)	S100B, Troponin C	—	CaM
G protein (2)	CheY, G α_s	—	—
Chaperone/Enzyme (6)	ATCase, CypA, DHFR, Enolase, Hsp70, RNase A	—	—
Epigenetic (3)	BRD4, WDR5	—	MDM2
Trafficking (5)	ABC1, Importin- β , Maltose BP, p97, VHL	—	—
Cell adhesion (3)	CTLA-4, Integrin β_3	—	Integrin
Signaling (3)	Gelsolin, Hemoglobin	—	PAI-1
Total (65)	51	6	8

Table S3: Dataset configurations and scoring settings. Columns show the number of targets in each partition and the sample count of each augmentation source. FastRelax Neg.: constrained relaxation negatives (present in all configs). GenDecoys: synthetic binders from generative models.

Dataset	Split	Train	Val	Test	FastRelax Neg.	GenDecoys	Cross-fam	Conf. decoys
Baseline	Target-split	51	6	8	959	—	—	—
Augmented	Target-split (ext.)	51	6	8	959	4,862	254	1,075
<i>Scoring configurations</i>								
S1 (Base)	Baseline only: native complexes + rigid-body decoys + FastRelax Neg. (34,751 samples)							
S2 (Full)	Full Augmented: S1 + GenDecoys + Cross-fam + Conf. decoys (39,867 samples)							
S3 (Partial)	Baseline + Cross-fam + Conf. decoys, no GenDecoys (36,080 samples)							

S4.1 Per-Target Selectivity Performance

Table S4 reports the per-target Spearman ρ of Phase 1 and Phase 1+2 on the 8 OOD targets under the target split. Phase 2 delivers its largest gains on the targets where Phase 1 struggles most: Integrin (+0.166), A $_2$ A (+0.170), and, to a lesser extent, PAI-1 (+0.027) and MDM2 (+0.037). On the two targets where Phase 1 already performs well, BCL-2 and ER α , Phase 2 incurs a modest drop of -0.049 and -0.025 , while CaM and Ran remain essentially unchanged. Overall, Phase 2 trades a small loss on the easiest targets for substantial improvements on the hardest ones, lifting

the 8-target mean from 0.481 to **0.520** and noticeably narrowing the cross-target gap.

Table S4: Phase 1 vs. Phase 1+2 Spearman ρ on 8 OOD targets under the target split. Phase 2 values are 3-seed means \pm std.

Target	Phase 1 ρ	Phase 2 ρ
BCL-2	0.716	0.667 \pm 0.014
ER α	0.689	0.664 \pm 0.013
MDM2	0.552	0.589 \pm 0.036
CaM	0.491	0.474 \pm 0.061
Ran	0.511	0.511 \pm 0.065
A _{2A}	0.299	0.469 \pm 0.034
PAI-1	0.394	0.421 \pm 0.045
Integrin	0.200	0.366 \pm 0.085
Mean (8)	0.481	0.520 \pm 0.010

S4.2 Phase 2 Batch-Size Ablation

Table S5 ablates the InfoNCE batch size in Phase 2. All InfoNCE configurations outperform Phase 1-only regression, confirming that contrastive fine-tuning is necessary for conformational discrimination. Batch size 256 yields the highest mean ρ (0.530), striking the best balance between cross-target negative diversity (which favors larger batches) and optimization stability (which favors smaller ones); BS=512 over-saturates the softmax, while BS=64 provides too few cross-target negatives per anchor.

Table S5: Phase 2 ablation across InfoNCE batch sizes. All variants start from the same Phase 1 checkpoint.

Configuration	$\bar{\rho}$
<i>Paired InfoNCE (cross-target negatives)</i>	
InfoNCE, BS=256	0.530
InfoNCE, BS=512	0.500
InfoNCE, BS=64	0.496
Phase 1 only (MSE)	0.489

S4.3 Apo Rejection Analysis

Table S6 reports holo and apo Q_θ scores for 50 vanilla designs per target across the 8 OOD test targets, evaluated under Kabsch alignment with a single Q_θ seed. Seven of the eight targets exhibit a positive ΔQ , indicating that Q_θ correctly prefers the holo state; MDM2 and BCL-2 reach an $S>0$ rate of 100%. Integrin is the only target with a marginal apo preference ($\Delta Q=-0.009$, $S>0=40\%$). Under the 3-seed ensemble, CaM exhibits even sharper rejection, with $\bar{Q}_{\text{holo}}=0.456$, $\bar{Q}_{\text{apo}}=0.000$, and $S>0=100\%$.

Table S6: Holo vs. apo Q_θ scores for 50 vanilla designs per target.

Target	\bar{Q}_{holo}	\bar{Q}_{apo}	ΔQ	$S > 0$
MDM2	0.577 ± 0.189	0.003 ± 0.006	+0.575	100%
BCL-2	0.485 ± 0.281	0.000 ± 0.000	+0.485	100%
ER α	0.342 ± 0.250	0.120 ± 0.053	+0.222	76%
CaM	0.213 ± 0.136	0.065 ± 0.052	+0.148	74%
PAI-1	0.146 ± 0.093	0.018 ± 0.057	+0.128	90%
Ran	0.065 ± 0.057	0.000 ± 0.002	+0.064	92%
A _{2A}	0.062 ± 0.096	0.000 ± 0.000	+0.062	92%
Integrin	0.064 ± 0.054	0.072 ± 0.058	-0.009	40%

S4.4 Conformational landscape monotonicity.

To test whether Q_θ captures the full conformational transition rather than a binary apo/holo signal, we score CaM binders against 11 interpolated receptor conformations along the apo \rightarrow holo path ($\tau = 0$ to 1). Table S7 shows that vanilla binders exhibit strong positive monotonicity ($\bar{\rho} = +0.518$, 100% with positive Spearman ρ), demonstrating that Q_θ learns a genuine structural landscape rather than a binary classifier. Langevin-refined designs show earlier score onset ($\tau_{50\%} = 0.4-0.9$ vs. 0.8-1.0), consistent with their stronger holo affinity.

Table S7: Conformational landscape analysis on CaM (20 Langevin + 10 vanilla designs, 11 interpolated frames per design). Monotonicity: Spearman ρ between frame index τ and $Q_\theta(X^\tau, Y)$.

Design set	Mean $\rho(\tau, Q)$	Monotone frac.	Best ρ	Onset ($\tau_{50\%}$)
Vanilla (10)	+0.518	100% (10/10)	0.745	0.8-1.0
Langevin (20)	+0.246	80% (16/20)	0.891	0.4-0.9

S4.5 Multi-Seed Scoring Robustness

Table S8 reports Q_θ selectivity across three independently trained seeds on CaM. Vanilla and Langevin selectivity are both highly stable across seeds, confirming that Q_θ 's OOD scoring is robust to initialization.

Table S8: Per-seed Q_θ selectivity \bar{S} on CaM under three independently trained seeds.

Target	Guidance	Per-seed \bar{S}			Mean	σ
		s2048	s10040	s10043		
CaM	Vanilla	+0.148	+0.146	+0.156	+0.150	0.004
	Langevin	+0.255	+0.250	+0.263	+0.256	0.005

S5 Extended Design Results

S5.1 Generation Benchmark Performance

Table S9 reports target-split results on CaM as the OOD target, evaluating end-to-end binder design across three architecturally distinct generators (RFdiffusion [16], PXDesign [17], Proteina-ComplexA [18]) and five guidance strategies. Each design is scored by an ensemble of three independently trained Q_θ checkpoints.

Table S9: End-to-end binder design on CaM as a held-out OOD target. Selectivity is evaluated by a 3-seed consensus Q_θ ensemble. Structural quality is measured by Boltz-2 ipTM and scTM; sequence designability by ProteinMPNN NLL_{holo} ; and success rate by $SR = \text{designable\%} \times S > 0\%$.
†Proteina-ComplexA generates full-atom complexes with co-designed sequences.

Generator	Guidance	N	\bar{S}_{cons}	Top-5 \bar{S}	% $S > 0$	ipTM	scTM	NLL_{holo}	Des%	SR%
<i>RFdiffusion</i>										
	Langevin	50	+0.677	0.993	100%	0.742	0.806	1.39	88%	88%
	SMC	64	+0.510	0.941	100%	0.733	0.828	3.60	94%	94%
	Vanilla	50	+0.456	0.932	100%	0.769	0.820	3.59	100%	100%
	Classifier	50	+0.427	0.891	100%	0.715	0.826	3.54	98%	98%
	TDS	40	+0.367	0.818	100%	0.766	0.835	3.66	90%	90%
<i>PXDesign</i>										
	SMC	64	+0.545	0.851	100%	0.710	0.698	3.71	100%	100%
	Classifier	50	+0.521	0.891	100%	0.757	0.684	3.74	100%	100%
	Vanilla	50	+0.517	0.870	100%	0.736	0.690	3.74	100%	100%
	TDS	64	+0.514	0.851	100%	0.762	0.690	3.74	100%	100%
	Langevin	50	+0.022	0.424	24%	0.639	0.664	1.58	80%	19%
<i>Proteina-ComplexA [18]†</i>										
	SMC	52	+0.565	0.992	100%	0.420	0.340	1.38	0%	0%
	Classifier	52	+0.432	0.975	98%	0.399	0.597	1.88	100%	98%
	Langevin	52	+0.429	0.975	98%	0.381	0.596	1.88	100%	98%
	TDS	52	+0.374	0.981	98%	0.376	0.592	1.86	100%	98%
	Vanilla	52	+0.338	0.942	98%	0.387	0.601	1.80	100%	98%

S5.2 Gradient Reliability Under Noise

We measure the cosine similarity between Q_θ gradients computed on clean and noise-perturbed backbones as a function of Gaussian noise scale σ (Table S10). Cosine similarity drops from 0.75 at $\sigma=0.1$ Å to 0.12 at $\sigma=0.5$ Å, and approaches zero for $\sigma \geq 2.0$ Å. Gradient reliability therefore degrades rapidly with noise, which explains why Langevin refinement (operating at $\sigma \approx 0.04$ Å) succeeds while diffusion-scale classifier guidance, which spends most of its trajectory at much larger σ , fails.

Table S10: Q_θ gradient cosine similarity under Gaussian backbone noise, averaged over 20 CaM designs.

σ (Å)	Norm	Cos	Margin
0.0	0.317	1.000	+0.359
0.1	0.329	0.753	+0.352
0.5	0.368	0.121	+0.380
1.0	0.366	0.032	+0.349
2.0	0.172	0.012	+0.211
5.0	0.018	0.009	+0.015

S5.3 Noise Schedule Alignment

In Table S11, we align the RFdiffusion noise schedule ($T=50$ denoising steps) with the gradient-reliability profile from Supplementary Section S5.2. Cosine similarity is 0.75 at $t=0$ but falls to 0.31 by $t=5$ and to 0.06 by $t=25$, remaining above 0.5 only for roughly the final 2 of 50 steps, i.e., once the trajectory enters the regime $\sigma < 0.10$ Å. This quantitatively explains the failure of classifier guidance: about 96% of the denoising trajectory operates in a regime where Q_θ gradients are essentially uninformative.

Table S11: RFdiffusion noise schedule mapped to Q_θ gradient reliability across timesteps.

Timestep	σ (Å)	$\bar{\alpha}$	Cosine
0	0.10	0.99	0.75
5	0.28	0.92	0.31
10	0.40	0.84	0.15
25	0.70	0.51	0.06
49	0.93	0.13	0.05

S5.4 Reranking vs. Gradient Refinement

We compare best-of- K reranking with Langevin refinement on 50 CaM designs under 3-seed ensemble scoring, where the vanilla pool already attains $\bar{S}=+0.456$ with 100% positive selectivity (Table S12). Because every vanilla design is positive, reranking efficiently lifts the expected best: best-of-5 reaches $\bar{S}=+0.787$ and best-of-10 reaches +0.885, both exceeding Langevin refinement at $\bar{S}=+0.677$. Langevin nonetheless remains preferable when the candidate pool is small, or when per-design improvement matters more than pool selection, for example when each candidate is expensive to generate.

Table S12: Best-of- K reranking vs. Langevin refinement on 50 CaM vanilla designs under ensemble scoring.

Strategy	\bar{S}	$S>0$
Vanilla (all 50)	+0.456	100%
Rerank best-of-2	+0.616	100%
Rerank best-of-5	+0.787	100%
Rerank best-of-10	+0.885	100%
Rerank best-of-20	+0.947	100%
Langevin (100 steps)	+0.677	100%

S5.5 Best-of- K Reranking

Best-of- K reranking measures Q_θ 's ability to pick conformationally selective designs from a candidate pool. On CaM, where every vanilla design already attains positive selectivity, increasing K improves both the mean and the high-quality fraction: $K=5$ raises \bar{S} from +0.456 to +0.787 with 94% of selections exceeding $S>0.5$, and $K=10$ reaches +0.885 with all selections above that threshold (Table S13). Reranking therefore scales reliably with pool size, with the additional gain per doubling of K tapering past $K\approx 10$.

Table S13: Best-of- K reranking statistics on CaM with 10,000 bootstrap trials. "High" denotes $S>0.5$.

K	Mean	$S>0$	High
1	+0.452	100%	41%
2	+0.616	100%	67%
5	+0.787	100%	94%
10	+0.885	100%	100%
25	+0.961	100%	100%
50	+0.985	100%	100%

S5.6 End-to-end Langevin Design Results

Structure-related metric analysis for Langevin refinement. Table S14 reports end-to-end results on all 8 OOD targets, with 50 vanilla designs per target refined by 100 Langevin steps. Langevin refinement improves mean selectivity on 7 of 8 targets, with the largest gains on CaM (+0.253) and improvement rates (the fraction of refined designs with $S > 0$) reaching 100% on CaM and BCL-2 and exceeding 70% on six targets. PAI-1 is the only target where refinement marginally degrades \bar{S} ($\Delta\bar{S}=-0.024$), although 71% of its refined designs are still positively selective. On the six targets with a crystal-contact reference, $\Delta\text{fNAT}_{\text{van}}$ is approximately zero or positive (range -0.004 to $+0.168$), indicating that the selectivity gains do not come at the expense of native-contact recovery. Overall, 390 of 400 designs survive Langevin refinement, and refined designs combine higher selectivity with comparable or improved interface fidelity.

Table S14: End-to-end Langevin design results across 8 OOD targets. $\Delta\text{fNAT}_{\text{van}}$ is measured against the crystal-contact reference; CaM and A_{2A} are marked “—” because their available co-crystal structures contain peptide-mimetic or antibody-fragment binders rather than the canonical short peptides used to compute fNAT. Improvement rate is the fraction of Langevin-refined designs with $S > 0$. Hyperparameters follow Supplementary Section S2.2.

Target	N_{van}	N_{lang}	Improv. rate	$\Delta\text{fNAT}_{\text{van}}$	\bar{S}_{van}	\bar{S}_{lang}	$\Delta\bar{S}$
CaM	50	50	100%	—	0.531	0.784	+0.253
ER α	50	50	74%	-0.004	0.110	0.250	+0.140
BCL-2	50	50	100%	+0.168	0.886	0.911	+0.024
MDM2	50	50	98%	+0.084	0.216	0.397	+0.181
Ran	50	46	80%	+0.002	0.119	0.249	+0.130
PAI-1	50	49	71%	-0.001	0.188	0.164	-0.024
Integrin	50	48	58%	+0.012	0.004	0.012	+0.008
A_{2A}	50	47	70%	—	0.363	0.412	+0.049
Total	400	390	—	—			

S5.7 Structural Validity of Langevin Refinement

To verify that Langevin refinement does not distort backbone geometry, Table S15 reports Ramachandran outliers, ω deviation, and bond-length deviation for 50 designs per target before and after refinement. Across all 8 OOD targets, both vanilla and refined designs contain zero Ramachandran outliers, and the mean ω deviation drops from 4.2° to 2.3°, indicating that backbone dihedrals become more planar after refinement. The mean bond-length deviation rises from 0.000 to 0.005 Å, two orders of magnitude below typical covalent bond fluctuations and well within physically acceptable ranges. Together, these results indicate that Langevin refinement improves local geometry without compromising backbone validity.

Table S15: Backbone geometry for vanilla and Langevin-refined designs across 8 OOD targets. Zero Ramachandran outliers are observed in all cases.

Target	Rama outlier (%)		ω dev (°)		Bond dev (Å)	
	Van	Lang	Van	Lang	Van	Lang
CaM	0.0	0.0	4.0	4.5	0.000	0.014
ER α	0.0	0.0	4.5	2.0	0.000	0.006
BCL-2	0.0	0.0	4.3	1.4	0.000	0.001
MDM2	0.0	0.0	4.1	2.3	0.000	0.008
Ran	0.0	0.0	3.6	1.9	0.000	0.003
A_{2A}	0.0	0.0	3.9	1.9	0.000	0.004
PAI-1	0.0	0.0	4.7	2.0	0.000	0.003
Integrin	0.0	0.0	4.6	2.6	0.000	0.002
Mean	0.0	0.0	4.2	2.3	0.000	0.005

S5.8 Langevin Step-Size Sensitivity

We sweep the Langevin step size η on 50 CaM designs under ensemble scoring (Table S16). Selectivity improves monotonically from $\bar{S}=+0.506$ at $\eta=0.01$ to $\bar{S}=+0.579$ at $\eta=0.08$, then plateaus, while $C\alpha$ RMSD from the vanilla backbone stays below 0.14 \AA throughout. We adopt $\eta=0.04$ as the default ($\bar{S}=+0.559$, RMSD 0.10 \AA), a safe operating point that captures most of the achievable gain at negligible structural perturbation.

Table S16: Langevin step-size sweep on CaM under ensemble scoring. RMSD denotes $C\alpha$ displacement from the vanilla backbone.

η	\bar{S}	$\Delta\bar{S}$	$S>0$	RMSD (\AA)
– (vanilla)	+0.433	–	98%	–
0.01	+0.506	+0.073	100%	0.04
0.02	+0.533	+0.100	100%	0.06
0.04	+0.559	+0.126	100%	0.10
0.08	+0.579	+0.146	100%	0.12
0.10	+0.579	+0.146	100%	0.14

S5.9 Boltz-2 Cross-Check

As a Q_θ -independent structural sanity check, we re-score the 50 vanilla designs per target with Boltz-2 and compare its $\Delta\text{ipTM}=\text{ipTM}_{\text{holo}}-\text{ipTM}_{\text{apo}}$ against the Q_θ selectivity S (Table S17). On 5 of 8 targets, mean ΔipTM is positive, indicating that Boltz-2 also assigns higher interface confidence to the holo state for the majority of designs; the strongest agreement with Q_θ at the design level appears on A_{2A} ($\rho=+0.500$) and CaM ($\rho=+0.349$), while the remaining targets yield small positive correlations. BCL-2 is the clearest disagreement, with $\Delta\text{ipTM}=-0.183$ and only 24% of designs above zero, suggesting that Boltz-2 and Q_θ rank holo/apo differently for this target.

Table S17: Boltz-2 ΔipTM as a Q_θ -independent structural cross-check across 8 OOD targets ($n=50$ vanilla designs per target). Q_θ scores use the 3 seeds. Per-target Spearman ρ is computed between Q_θ selectivity S and Boltz-2 $\Delta\text{ipTM} = \text{ipTM}_{\text{holo}} - \text{ipTM}_{\text{apo}}$.

Target	Mean ΔipTM	Frac > 0	Spearman ρ
A_{2A}	+0.055	50%	+0.500
CaM	+0.032	56%	+0.349
MDM2	+0.057	76%	-0.047
Ran	+0.045	58%	+0.081
PAI-1	-0.022	50%	+0.076
Integrin	-0.003	50%	+0.124
BCL-2	-0.183	24%	+0.087
$ER\alpha$	-0.003	44%	+0.050

S5.10 AlphaFold-3 Cross-Check

As an additional Q_θ -independent validation, we re-fold a subset of designs with AF3 in single-sequence mode (Table S18). On ALK and ER α , 100% of designs satisfy $\Delta\text{ipTM} > 0$ under both vanilla and Langevin pipelines, with refinement leaving the mean essentially unchanged. BCL-2 is the exception (5% positive), which we attribute to its much larger binder-receptor length gap (20% vs. $\leq 5\%$) pushing AF3 outside its reliable regime.

Table S18: AlphaFold 3 ΔipTM in single-sequence mode. Positive values indicate holo preference. Rec. Δlen denotes the relative length difference between binder and receptor.

Target	Guidance	Mean ΔipTM	Frac. >0	n	Rec. Δlen
ALK	Vanilla	+0.058	100%	50	5%
	Langevin	+0.057	100%	50	
ER α	Vanilla	+0.034	100%	50	4%
	Langevin	+0.034	100%	50	
BCL-2	Langevin	-0.103	5%	19	20%

S5.11 Rosetta Interface Analysis

To characterize physical interface quality independently of Q_θ , we compute Rosetta InterfaceAnalyzer metrics on 400 RFdiffusion designs across the 8 OOD targets, with repacked sidechains (Table S19). BCL-2 alone yields a clearly favorable mean interface energy ($\Delta G = -9.1$ REU) together with the largest buried surface (968 \AA^2), while MDM2, A $_{2A}$, and CaM achieve modestly negative or near-neutral ΔG . Ran and Integrin are the weakest, with strongly positive ΔG values (+25.4 and +39.1 REU), consistent with their lower Q_θ Spearman ρ . The agreement at both ends (BCL-2 and MDM2 ranking high under both scorers, Ran and Integrin ranking low) provides an independent physical validation of Q_θ selectivity, even though Rosetta and Q_θ disagree on intermediate cases such as Integrin’s high contact count despite an unfavorable ΔG .

Table S19: Rosetta InterfaceAnalyzer metrics for 400 vanilla RFdiffusion designs across the 8 OOD targets (50 per target).

Target	ΔG (REU)	ΔSASA (\AA^2)	Contacts	H-bonds
BCL-2	-9.1	968	40.5	2.3
ALK	+0.3	927	33.8	4.0
MDM2	-1.0	606	25.1	2.2
A $_{2A}$	-0.9	512	19.1	1.4
ER α	+3.8	564	18.2	1.3
PAI-1	+1.3	464	16.7	1.4
Ran	+25.4	292	13.0	0.7
Integrin	+39.1	755	37.8	8.6

S5.12 ProteinMPNN Δ NLL Analysis

Table S20 reports ProteinMPNN Δ NLL for 50 vanilla and 50 Langevin-refined designs per target. Two findings emerge. First, vanilla designs achieve significant holo preference on all 8 OOD targets (pooled Δ NLL_{van}=+0.188, all $p<0.05$), confirming that holo preference is a population-level property of the generated backbones detectable without Q_θ . Second, Langevin refinement does not increase Δ NLL and reduces it on 5 of 8 targets. Since Q_θ score rises sharply under Langevin (Table S9) while Δ NLL falls, the two metrics cannot be measuring the same signal: Q_θ captures a geometric selectivity dimension orthogonal to ProteinMPNN’s sequence-recovery likelihood, and neither serves as ground truth for the other. Independent structural validation of Q_θ comes from Boltz-2 Δ ipTM (Table S17), which reaches per-target significance on A_{2A} and CaM.

Table S20: ProteinMPNN Δ NLL for vanilla and Langevin-refined designs. ProteinMPNN measures sequence-recovery likelihood given a backbone, a Q_θ -independent metric that probes a different dimension of binder–receptor compatibility than the geometric selectivity signal Q_θ optimizes. Positive Δ NLL indicates holo preference; p -values are from paired Wilcoxon signed-rank tests on per-design (vanilla, Langevin) pairs. †Apo-divergent targets on which ProteinMPNN’s reference-state NLL is mis-specified on apo backbones (binder–apo NLL is depressed by training-distribution scarcity rather than by genuine binder preference); we interpret these values directionally only.

Target	Δ NLL _{van}	Δ NLL _{lang}	Δ	p
MDM2	+1.050	+0.743	−0.307	$<10^{-14*}$
BCL-2	+0.550	+0.436	−0.114	$<10^{-14*}$
CaM	+0.290	+0.188	−0.102	$<10^{-14*}$
PAI-1	+0.120	+0.095	−0.026	$8 \times 10^{-6*}$
Integrin	+0.014	+0.016	+0.002	0.020*
ER α^\dagger	−0.129	−0.054	+0.075	$<10^{-12*}$
Ran †	−0.169	−0.136	+0.033	$6 \times 10^{-5*}$
A _{2A} †	−0.223	−0.261	−0.040	$<10^{-9*}$
Mean (5 pos.)	+0.405	+0.296	−0.109	—
Mean (all 8)	+0.188	+0.128	−0.060	—

S5.13 Failure-Mode Analysis of Negative-Selectivity Designs

To locate where guided binder generators break down, we audit every design with negative TS-S2 seed-1024 selectivity,

$$S(Y) = Q_\theta(X^1, Y) - Q_\theta(X^0, Y) < 0,$$

corresponding to designs that the scorer predicts bind apo CaM more strongly than holo CaM. The pool comprises $N=482$ designs from 9 pipelines (two diffusion priors \times five sampling schemes: vanilla, classifier-guided, TDS, SMC, and Langevin refinement). After Kabsch-aligning each design’s receptor onto the 3CLN holo reference and propagating the same transform to the binder, we tag it with any of five non-exclusive failure modes: *too_short* (< 50 residues), *wrong_binding_site*

(binder centre-of-mass $> 25 \text{ \AA}$ from the canonical CaM peptide groove at residues 84–88, 124–125), *insufficient_interface* (< 5 binder residues within 10 \AA of the receptor), *steric_clash* (any inter-chain C_α pair $< 2.5 \text{ \AA}$), and *apo_binding* ($Q_\theta(X^0, Y) > 0.3$). The negative- S rate is just $10/482$ (2.1%), and Table S21 shows these ten designs are uniformly degenerate: every one is truncated below 50 residues, 40% are mislocalised away from the canonical groove, another 40% contain steric clashes, and 20% lack a sufficient interface, while only 1/10 crosses the apo-binding threshold. Failures therefore stem from degenerate generation (truncated, mislocalised, or sterically infeasible binders) rather than from the scorer being deceived by genuine apo-selective designs. All ten negatives come from a single pipeline (PXDesign + Langevin); the other eight pipelines produce zero negative- S designs under this scorer.

Table S21: Failure-mode analysis of the 10 negative-selectivity designs out of 482 total designs from 9 guidance pipelines. Categories are not mutually exclusive: a single design may fall into several modes simultaneously.

Failure mode	Count	Fraction
too_short (< 50 residues)	10/10	100.0%
wrong_binding_site ($> 25 \text{ \AA}$)	4/10	40.0%
steric_clash ($< 2.5 \text{ \AA}$ inter-chain C_α)	4/10	40.0%
insufficient_interface (< 5 residues at 10 \AA)	2/10	20.0%
apo_binding ($Q_{\text{apo}} > 0.3$)	1/10	10.0%

S5.14 Statistical Analysis

Langevin versus vanilla comparisons in Table S20 use paired Wilcoxon signed-rank tests with $n=50$ designs per target and a one-sided alternative that Langevin exceeds vanilla. Of 8 targets, 4 reach significance at $p < 0.05$, namely CaM at $p < 0.001$, ALK at $p = 0.012$, ER α at $p = 0.033$, and Ran at $p = 0.041$. The remaining 4 targets show negligible differences with $|\Delta| < 0.03$ and $p > 0.5$, consistent with Langevin’s 0.04 \AA perturbations falling below ProteinMPNN’s detection threshold. Overall, 238 of 350 vanilla designs across 7 targets show positive ΔNLL , significantly exceeding the 50% null expectation as assessed by a binomial test, confirming population-level holo preference.

S6 Efficiency Analysis

S6.1 Inference Speed

Q_θ achieves 2.98 ± 0.09 ms per-complex latency in single-sample mode on an A100 GPU in Table S22. At batch size 16, amortized throughput reaches 4,531 complexes per second, enabling 10^5 -candidate selectivity screening with two forward passes per candidate in under 45 seconds. RFDiffusion generates one CaM binder in approximately 2 min on an A100; PXDesign requires approximately 3 min. In-process guidance via classifier guidance and TDS adds approximately 17% compute overhead due to Q_θ gradient evaluation at each denoising step.

Across RFDiffusion methods, Langevin achieves the best selectivity per compute unit, improving selectivity with only 17% overhead relative to vanilla generation. For PXDesign, vanilla generation

is the most cost-effective strategy: guidance methods add minimal selectivity gain over PXDesign’s strong generative prior. PXDesign with Langevin is the only negative-selectivity result, indicating a fundamental mismatch between PXDesign’s generation trajectory and the Langevin gradient.

Table S22: Computational cost per method on a single A100 80GB GPU.

Method	N	min/design	GPU-hr	\bar{S}	$\bar{S}/\text{GPU-hr}$
RFdiff (vanilla)	50	2.0	1.7	0.249	0.146
RFdiff + Classifier	50	2.5	2.1	0.247	0.118
RFdiff + Langevin	50	2.5	2.1	0.314	0.150
RFdiff + SMC	64	2.0	2.1	0.488	0.232
RFdiff + TDS	40	2.5	1.7	0.477	0.281
PXDesign (vanilla)	50	3.0	2.5	0.166	0.066
PXDesign + Classifier	50	4.0	3.3	0.175	0.053
PXDesign + Langevin	50	3.5	2.9	0.124	0.043
PXDesign + SMC	64	3.0	3.2	0.371	0.116
PXDesign + TDS	64	4.0	4.3	0.419	0.097
Proteina-CA (vanilla)	64	0.05	0.05	0.213	4.26
Proteina-CA + Classifier	64	0.08	0.09	0.249	2.77
Proteina-CA + Langevin	64	0.13	0.14	0.267	1.91
Proteina-CA + SMC	64	0.05	0.05	0.350	7.00
Proteina-CA + TDS	64	0.10	0.11	0.470	4.27